metals

MDPI

Article

Thermodynamic Analysis for the Magnetic-Field-Induced Precipitation Behaviours in Steels

Zihua Li, Tingping Hou *, Guanghui Wu, Kaiming Wu * and Hengfu Lin

The State Key Laboratory for Refractories and Metallurgy, Hubei Province Key Laboratory of Systems Science in Metallurgical Process, International Research Institute for Steel Technology, Wuhan University of Science and Technology, Wuhan 430081, China

* Correspondence: houtingping@wust.edu.cn (T.H.); wukaiming@wust.edu.cn (K.W.); Tel.: +86-1814-052-2212; (T.H.); +86-1310-061-0041 (K.W.); Fax: +86-27-68862606 (T.H.); +86-27-68862606 (K.W.)

Received: 24 July 2019; Accepted: 13 August 2019; Published: 19 August 2019

Abstract: Alloy carbide $M_{23}C_6$ plays a significant role in the creep strength of reduced activation steels. Experiments have proven that a magnetic field accelerates the precipitation of $M_{23}C_6$ at intermediate temperature. A scheme that combines first-principle calculations, Weiss molecular field theory and equilibrium software MTDATA is proposed to investigate the thermodynamic features of magnetic-field-induced precipitation. The calculated results reveal that the origin of the magnetic moment is the NaCl-like crystal structure. The magnetic field enhances the exchange coupling and stabilizes the ferromagnetic phase region. The external field influences the Curie temperature, thereby changing the magnitude and position of the maximum magnetic heat capacity, magnetic entropy and enthalpy. The strong magnetic field improves the stability of $M_{23}C_6$, and the theoretical results agree well with the previous experiment. The study provides a theoretical basis for the magnetic-field-induced precipitation behaviours in steels.

Keywords: steel; carbide; high magnetic field; magnetic moment; thermodynamic properties

1. Introduction

In recent decades, the precipitation behavior of iron or alloy carbides induced by an external magnetic field has aroused great interest. First, experimental studies [1,2] were performed to discuss the impact of magnetic field on iron carbides. It was found that the magnetic field stabilizes ferromagnetic iron carbide (χ-Fe_5C_2), which can be magnetized under a magnetic field. Second, alloy carbides M_6C (M = Fe, Mo) precipitated in advance with a magnetic field [3]. Similarly, the external field accelerates the precipitation of $M_{23}C_6$ (M = Cr, Fe) [4]. The precipitation behavior of carbide is closely related to its stability. With a magnetic field, the stability of carbides was ascribed to the reduction of free energy related to magnetization [1,2,5]. Moreover, the magnetic field influences the morphologies of precipitated carbides [6,7]. It was demonstrated that carbides spheroidized under a magnetic field, driven by interfacial energy and magnetostrictive strain energy. Many works have explained the precipitation of carbides from the perspective of magnetic free energy [4,8]. Although thermodynamic contributions which derived by magnetization to free energy have been taken into account in many studies [5,9], other thermodynamic properties (e.g., heat capacity, entropy and enthalpy) have yet to be studied at the microscopic level.

The stable alloy carbide $M_{23}C_6$ [10] has been observed in steels [8,11]. The stability of $M_{23}C_6$ has been determined by first-principle calculations. It was indicated that the stability of alloy carbides containing Cr is greater than that of other $M_{23}C_6$ (M = Fe or Ni) carbides [12]. Calculations have indicated that $Cr_{23}C_6$ is a stable carbide due to its negative formation energy [13]. When Cr atoms are

replaced by Fe atoms, it becomes an alloy carbide. For alloy carbides $(Fe, Cr)_{23}C_6$, the concentration of Cr and magnetism will influence the stability of carbides [12]. The calculated stability of alloy carbides can to some extent provide a reference for experiments. Ferromagnetic carbides can be significantly affected with application of a magnetic field. The chromium carbide $Cr_{23}C_6$ is nonmagnetic [13], whereas $Fe_{23}C_6$ is magnetic with a large magnetic moment [8,14]. The magnetic moment of $(Fe, Cr)_{23}C_6$ varies with respect to the iron concentration. However, first-principle calculations are limited to the ground state properties of carbides (0 K, 0 Pa). Further research is needed to explore the properties of carbides under realistic processing conditions, especially with magnetic fields and different temperatures.

In the present paper, the mechanism of carbide precipitation with a high magnetic field is investigated from the perspective of thermodynamics based on existing experimental results [4]. The magnetic moments are obtained by first-principle calculations, and the relationship between the magnetic moment and the structure of $Fe_{20}Cr_3C_6$ has been investigated. The ground state magnetic moments are combined with the Weiss molecular field theory, and the effects of the magnetic field on the magnetic moment evolution and Curie temperature are determined. Then, the magnetic free energy which is derived by magnetic heat capacity, magnetic entropy and magnetic enthalpy are analyzed. The results (including magnetic and thermal free energy) can accurately describe the experimental carbide precipitation behaviour under a magnetic field, which can further elaborate the thermodynamic mechanisms of precipitation.

2. Experiment Procedures

The chemical composition (wt %) was 0.1C-2.2Cr-1Mo-0.5Mn-0.3Si (2.25Cr-Mo). It is a typical intermediate temperature heat resistant steel. The alloy design and heat treatments were introduced in the previous work [4]. The magnetic field was applied during tempering at 823 K (550 °C) for 1 h (3600 s). The results are shown in Table 1.

Table 1. The carbide types formed during tempering at 823 K for 1 h with and without 12 T magnetic field.

Magnetic Field Strength (T)	Precipitation Types
0	M_2C, M_3C
12	M_2C, M_3C, M_7C_3, $M_{23}C_6$

In the absence of the 12 T magnetic field, M_2C (η-Fe_2C) and M_3C (θ-Fe_3C) precipitated. However, M_7C_3 and $M_{23}C_6$ precipitated with M_2C and M_3C under a magnetic field. In the traditional heat treatment process, the precipitation of M_7C_3 and $M_{23}C_6$ may require higher temperature (>600 °C) or longer time (>100 h) [15,16]. Thus, a magnetic field remarkably made $M_{23}C_6$ and M_7C_3 precipitate in advance. This article focuses on the thermodynamic mechanism that the precipitation of $M_{23}C_6$ promoted by the magnetic field. More than 50 isolated particles were selected to examine the composition of $M_{23}C_6$ by gold replica specimens [4]. The experimental concentration in $M_{23}C_6$ was $Fe_{19.58}Cr_{3.42}C_6$. However, the model of $Fe_{19.58}Cr_{3.42}C_6$ is difficult to construct, because the occupation of iron and chromium atoms is difficult to be accurate to decimals. The composition of $Fe_{19.58}Cr_{3.42}C_6$ is close to that of $Fe_{20}Cr_3C_6$. Consequently, the model of $Fe_{20}Cr_3C_6$ was used to calculate its properties instead of the experimental result ($Fe_{19.58}Cr_{3.42}C_6$) in the subsequent calculations.

3. Methods

It is difficult to synthesize pure $M_{23}C_6$ by the experimental method and almost impossible to measure its magnetic properties. In order to explain the previous experimental results, the present work takes advantage of the first-principle calculations to get the ground state (0 K, 0 T) magnetic moment. Then, the magnetic moment (internal magnetism) was expanded by the Weiss molecular field theory (Supplementary note 2). Based on the above calculation results, the internal magnetic properties

combined with magnetic-field-induced magnetism was used to determine the thermodynamic parameters of alloy carbides. Finally, the experimental phenomena can be explained by change of the Gibbs free energy.

The $M_{23}C_6$ carbide belongs to the cubic space group Fm-3m (225). Figure 1 shows the crystal structure of $M_{23}C_6$, which contains five nonequivalent Wyckoff sites (metal and carbon sites 24e). Metal sites are 4a, 8c, 32f and 48h [17,18]. For $Fe_{20}Cr_3C_6$, iron atoms occupy 32f and 48h sites (Fe32f indicates that Fe occupies the 32f site, and subsequent descriptions are also described in similar ways), which form a closely linked framework [9,14]. Chromium atoms occupy 4a and 8c sites.

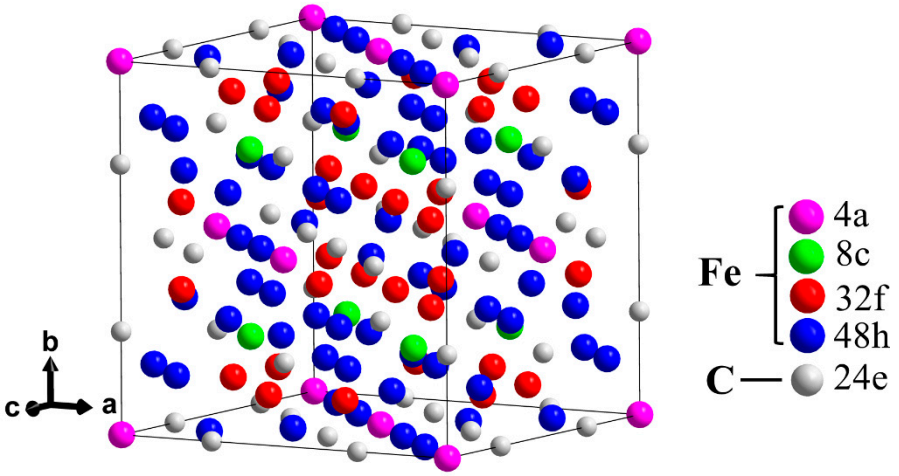

Figure 1. (Color online) Schematic crystal structure of $Fe_{23}C_6$ with five nonequivalent Wyckoff sites, wherein the metal sites are occupied by Fe atoms, and C atoms occupy the 24e sites.

In the present work, the ground state properties are calculated within the framework of the density function theory [19] as implemented in the Vienna Ab-initial Simulation Package (VASP) [20–22]. Instead of local-(spin-polarized) density approximation, the exchange-correlation potential was described by the generalized gradient approximation [12,23] which was formulated by Perdew, Burke and Ernzerhof [24]. The valence electron configurations are treated as $3d^74s^1$ for Fe, $3d^54s^1$ for Cr and $2s^2p^2$ for C. The cut-off energy was 400 eV for η-Fe_2C and θ-Fe_3C, 500 eV for $Fe_{23}C_6$ and $Fe_{20}Cr_3C_6$. The k-point mesh was $5 \times 6 \times 8$, $5 \times 4 \times 6$, $5 \times 5 \times 5$, $5 \times 5 \times 5$ for η-Fe_2C, θ-Fe_3C, $Fe_{23}C_6$ and $Fe_{20}Cr_3C_6$, respectively, using the Monkhorst-Pack method [25]. Those tests of k-mesh and cut-off energies showed good convergence (<1 meV/atom). Structure optimizations were executed for both lattice parameters and coordinates of atoms.

4. Results and Discussion

4.1. Identification of the $M_{23}C_6$

Figure 2a shows the selected area electron diffraction (SAED) of $M_{23}C_6$ from the experiment. Figure 2b shows the SAED pattern of $Fe_{20}Cr_3C_6$ from the simulation, which agrees well with the experiment. According to the electron scattering factors and structure factors of the diffraction (Supplementary note 1), the related parameters are defined, and the model is established to reflect the diffraction pattern of the crystal in detail. By inputting the zone axis and the coordinates of the atoms in the crystal, the diffraction patterns that vary with the input parameters have been displayed. In Figure 2b, the point with a large area corresponds to a diffraction spot with a strong intensity. The experimental angle of (111) and (−220) is 90.47°, which is in agreement with the theoretical value 90°. There is a little difference in the experimental and simulated intensities because the theoretical results are obtained under ideal conditions and the kinetic interaction between electrons is not considered.

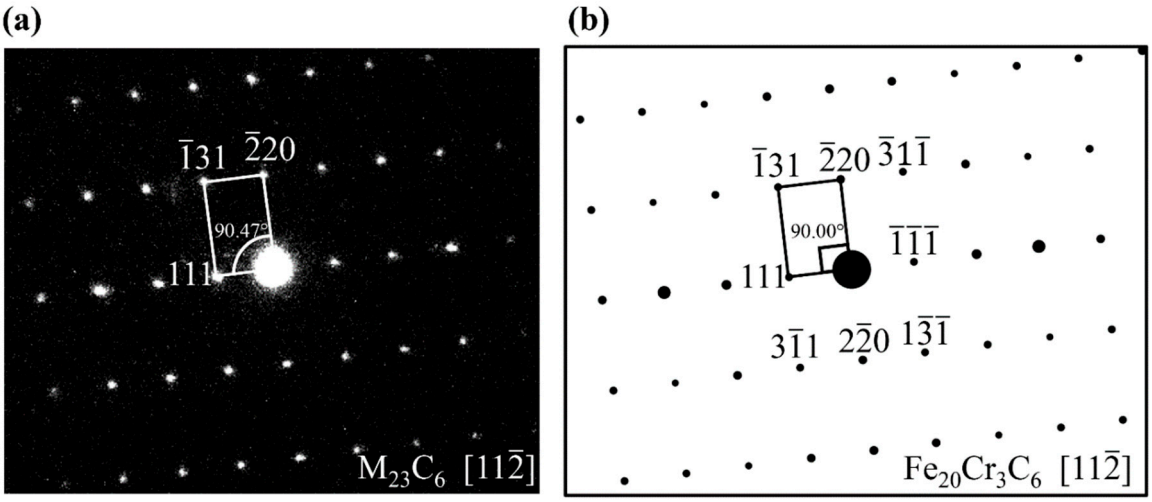

Figure 2. (**a**) Selected area electron diffraction (SAED) pattern of the experimental results [4]. Observation of carbon replicas tempered at 823 K for 1 h with a 12 T magnetic field. $M_{23}C_6$ was identified by using its cubic unit cells; (**b**) simulated SAED pattern of $Fe_{20}Cr_3C_6$ along [11$\bar{2}$] zone axes. The intensity of the diffraction spot is proportional to its area.

4.2. Basic Structure and Ground State Magnetism

Figure 3b shows the simplified structure of $Fe_{20}Cr_3C_6$, which consists of polyhedrons (centered on Cr4a atoms), cubes (composed of Fe32f atoms) and octahedrons (composed of C24e atoms) in Figure 3a. The Cr4a atom forms a polyhedron with the surrounding 12 Fe48h atoms. The cuboctahedron is formed by a cube nesting together with an octahedron. Cr8c atoms are in the interstitial site of the infrastructure. The arrangement of basic structures (Figure 3a) is similar to NaCl. The crystal structure of $Cr_{23-x}Fe_xC_6$ (x = 0–3) in which the Fe atoms partially occupied the single Wyckoff sites, has been proven that its structure is similar to NaCl [26]. In the present work, the simplified structure like NaCl is found in $Fe_{20}Cr_3C_6$.

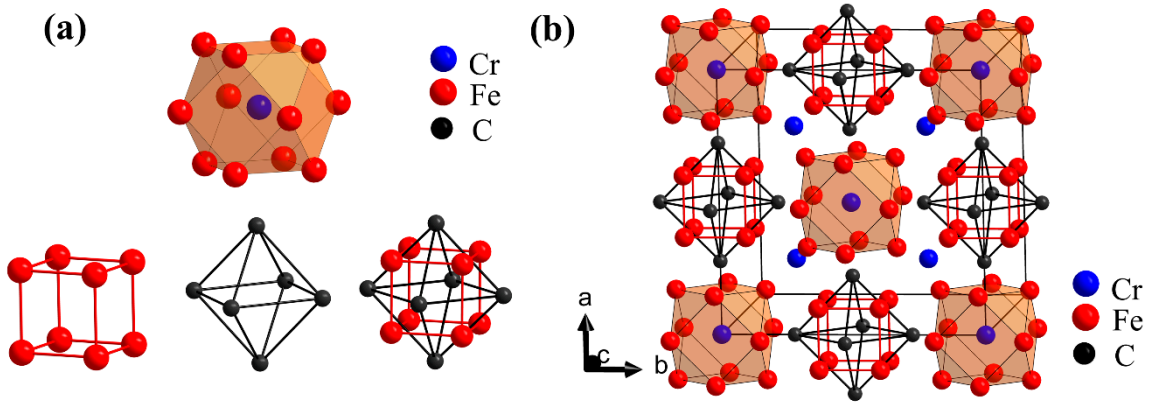

Figure 3. (Color online) (**a**) Cr4a-Fe48h polyhedron and Fe32f-C24e cuboctahedron in $Fe_{20}Cr_3C_6$. The Cr4a-Fe48h polyhedron is composed of a centrally located Cr4a atom and 12 nearest neighbor Fe48h atoms. The Fe32f-C24e cuboctahedron comprises a Fe32f cube and C24e regular octahedron nested through a shared center; (**b**) Simplified structure of $Fe_{20}Cr_3C_6$. The structure cell consists of polyhedrons and cuboctahedrons. The arrangement of the basic structures is similar to NaCl, and Cr8c is positioned at the interstitial site.

The magnetic properties of iron carbides have been analyzed by first-principle calculations [14,27,28]. The iron carbides exhibit a ferromagnetic state, but the substitution of Fe by Cr may change magnetism. The calculations were performed on $Fe_{23}C_6$ to ensure the calculation accuracy; the results are listed in Table 2. The lattice parameter agrees well with the experimental and

theoretical values [14,29–31] within the range of error. Comparing the magnetic moments of atoms in $Fe_{23}C_6$ and $Fe_{20}Cr_3C_6$ (Table 2), the magnetic moments of chromium are antiparallel to those of iron. The local magnetic moments of iron in $Fe_{23}C_6$ is larger than that of iron in $Fe_{20}Cr_3C_6$. The Cr4a atom is surrounded by Fe atoms (Figure 3a) in $Fe_{20}Cr_3C_6$. Each antiparallel magnetic moment of Cr atom would reduce the magnetic moment of the surrounding iron atoms [9], resulting in a smaller magnetic moment of iron in $Fe_{20}Cr_3C_6$. The magnetic moment of carbide is not only related to Cr atoms but also to multiple factors, such as Wyckoff sites and bond distances [9]. For $Fe_{20}Cr_3C_6$, the total magnetic moment is mainly contributed by Fe48h and Fe32f. However, the magnetic moments of Fe48h and Fe32f in $Fe_{20}Cr_3C_6$ are 3.0% and 16.7% less than those in $Fe_{23}C_6$, respectively (Table 2). The magnetic moment of the C atom is negative and can influence the magnetic properties of other atoms. In $Fe_{20}Cr_3C_6$, the difference of Fe48h-C (2.0865 Å) and Fe32f-C (2.0512 Å) bond lengths is not significant, the interaction of C and Fe is similar. The Fe48h nearest neighbours have Cr4a and Cr8c, whereas the Fe32f nearest neighbours have only Cr8c. The bond length of Fe48h-Cr4a, Fe48h-Cr8c and Fe32f-Cr8c is 2.4939 Å, 2.8619 Å and 2.3955 Å, respectively. Since the bond length of Fe32f and Cr8c is the shortest, there will be strong interactions between atoms (Fe32f and Cr8c), resulting in a significant decrease in the magnetic moment of Fe32f.

Table 2. Calculated lattice parameters, local magnetic moment and energy per formula for $Fe_{23}C_6$ and $Fe_{20}Cr_3C_6$. The lattice parameter is compared with theoretical values calculated by Vienna Ab-initial Simulation Package (VASP) [14,29] and Cambridge Serial Total Energy Package (CASTEP) [30,31].

Carbides	Space Group	Lattice Parameters (Å)	Magnetic Moment (μ_B/atom)	Energy (eV/f. u.)
$Fe_{23}C_6$	Fm-3m (225)	10.38 10.47 [14] 10.46 [29] 10.05 [30] 10.16 [31]	4a: 2.33 2.53 [14] 8c: 2.72 2.82 [14] 32f: 1.67 1.78 [14] 48h: 2.04 2.15 [14] 24e: −0.12 −0.15 [14]	−241.875 −245.238 [14]
$Fe_{20}Cr_3C_6$	Fm-3m (225)	10.41	4a (Cr): −2.20 8c (Cr): −2.16 32f: 1.39 48h: 1.97 24e: −0.10	−247.670

Table 3 shows the magnetic moments of η-Fe_2C, θ-Fe_3C, $Fe_{23}C_6$ and $Fe_{20}Cr_3C_6$. The alloy carbides exhibit pronounced magnetic moments, which means that they are ferromagnetic. The magnetic state of $Fe_{20}Cr_3C_6$ does not change when the Fe atoms are partially replaced by the Cr atoms in $Fe_{23}C_6$. Since η-Fe_2C, θ-Fe_3C and $Fe_{20}Cr_3C_6$ are ferromagnetic, the application of an external magnetic field can affect the magnetic behaviors.

Table 3. Magnetic moments of η-Fe_2C, θ-Fe_3C, $Fe_{23}C_6$ and $Fe_{20}Cr_3C_6$ (μ_B per formula).

Carbides	Magnetic Moment (μ_B/f. u.)
η-Fe_2C	3.22–3.34 [28]
θ-Fe_3C	5.70–5.77 [28]
$Fe_{23}C_6$	46.73
$Fe_{20}Cr_3C_6$	28.91

4.3. Magnetism Dependence on an External Field

Since the first-principle calculation is limited to the ground state, the ground state magnetic moment is a fixed value. In fact, the magnetic moment varies with respect to the temperature and external field [5]. The introduction of the Weiss molecular field theory (Supplementary note 2) [32] can expand the ground state magnetic moment to a wide temperature. The ground state magnetic moments of alloy carbides are taken as initial parameter of Weiss molecular field theory (Equation (S3)

in Supplementary note 2). Then, the magnetic properties that depend on the temperature and magnetic field can be derived by magnetization (see Equation (1)).

$$m\ (T, B) = M\ (T, B)/(N \cdot \mu_B) \quad (1)$$

where m (T, B) is the magnetic moment and M (T, B) is the magnetization. Both m and M are functions of B (the strength of the external field) and T (temperature), N is the number of atoms per unit volume, and μ_B is the Bohr magneton.

The magnetic moments of η-Fe_2C, θ-Fe_3C, $Fe_{23}C_6$ and $Fe_{20}Cr_3C_6$ were calculated with and without a 12 T magnetic field (Figure 4). Compared to the m (T, 0 T) with m (T, 12 T), the magnetic moments are identical below approximately 200 K. When the temperature is higher than 200 K, the magnetic moments gradually decrease to zero without a magnetic field. Since the increase of temperature decreases the exchange coupling and thermal motion constantly destroys the regular orientation of atomic magnetic moments. The applied 12 T magnetic field forces the magnetic moment to align with the direction of the external field, increasing the exchange effect. Consequently, when the temperature is above 200 K, the magnetic moment under the external field is larger than that without the magnetic field.

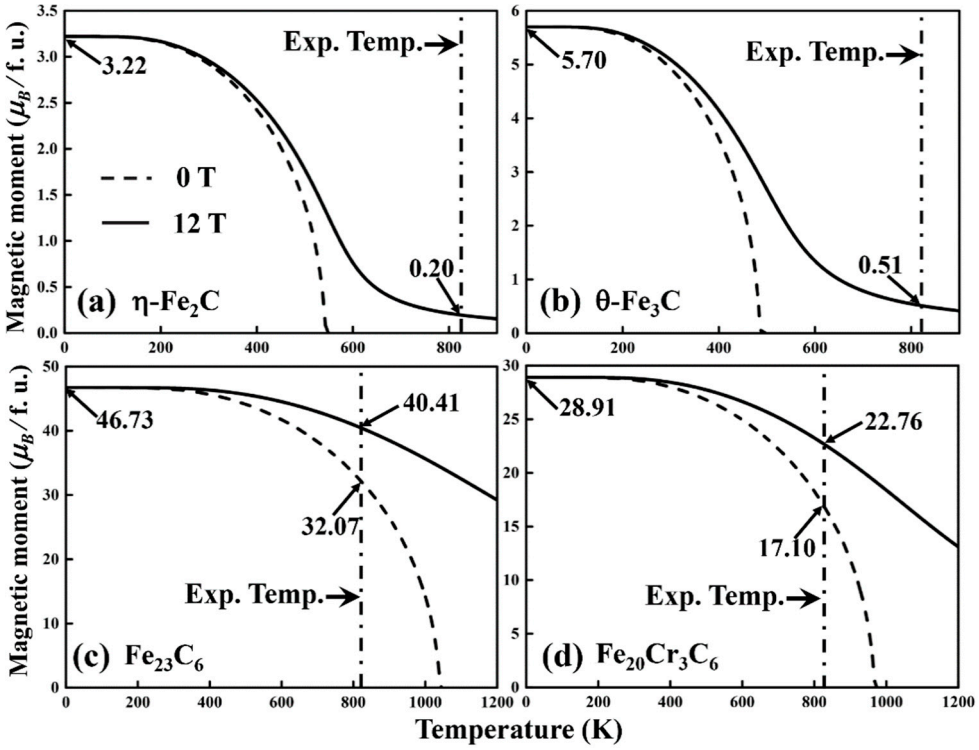

Figure 4. Magnetic moments of (**a**) η-Fe_2C, (**b**) θ-Fe_3C, (**c**) $Fe_{23}C_6$ and (**d**) $Fe_{20}Cr_3C_6$ with (solid lines) or without a magnetic field (dash lines). The arrows indicate the magnetic moments determined by first-principle calculations (T = 0 K), the magnetic moments of carbides at 823 K (550 °C) without a magnetic field (B = 0 T) and the magnetic moments at 823 K (550 °C) with a magnetic field (B = 12 T), respectively.

4.4. Influence of the Magnetic Field on the Curie Temperature

Generally, the Curie temperature T_c is the critical temperature at which spontaneous magnetization disappears. T_c increases with increasing intensity of the applied field for pure iron [33]. T_c of 3d transition metal substitutional alloys has been calculated by first-principle calculations [34], and the

results show that the increase in T_c is related to the increase in the exchange coupling constant between Fe atoms. In the present study, T_c (B) is defined as the inflection point of the magnetization curve:

$$\frac{\partial^2 M(T,B)}{\partial T^2} = 0 \tag{2}$$

Figure 5 shows the change of T_c under different magnetic fields. The results show that the Curie temperature of alloy carbides increases as the magnetic field strength increases, which is similar to the literature [5,33]. The variation in T_c with regard to the external field strength is closely related to the magnetic moment of the alloy carbide. The changes of $Fe_{23}C_6$ and $Fe_{20}Cr_3C_6$ are greater than those of η-Fe_2C and θ-Fe_3C, which is closely related to the magnetic moment of the alloy carbide and magnetic field strength. The higher magnetic field strength would enhance the exchange interaction between parallel magnetic moments [33], which can stabilize the ferromagnetic state. The results reveal that the external field can enlarge the ferromagnetic region. Consequently, the temperature range of carbide precipitation will also change under the magnetic field.

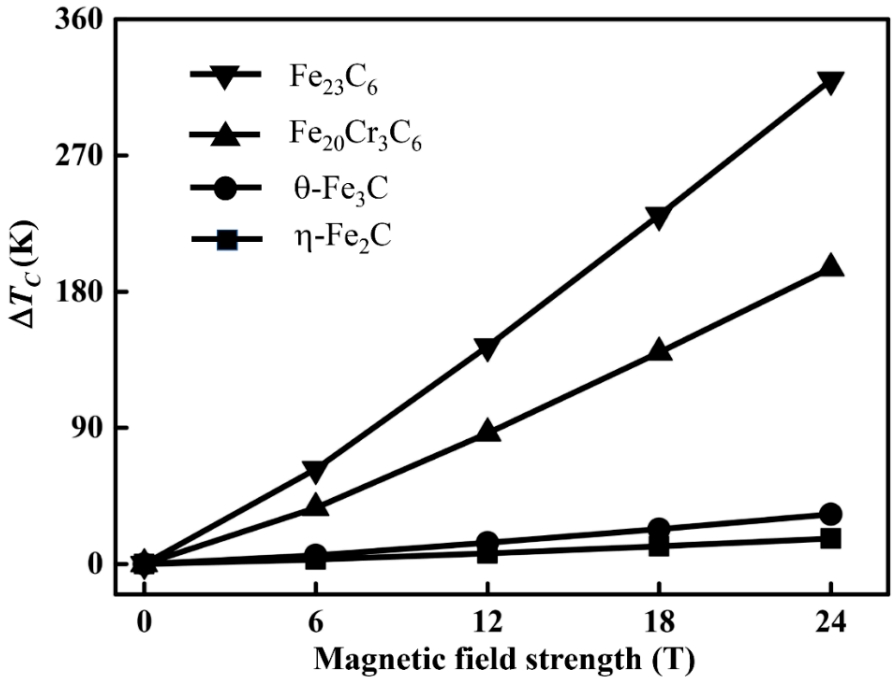

Figure 5. The change of Curie temperature ($\Delta T_c\ (B) = T_c\ (B) - T_c\ (0)$ of carbides under various external magnetic fields.

4.5. Thermodynamic Analysis in Magnetic Field

As an important thermodynamic parameter, heat capacity is closely related to material structure and energy. It is generally known that the heat capacity (or entropy) is closely related to lattice contribution, electronic contribution and magnetic contribution [35,36]. The lattice heat capacity (or lattice entropy) and electronic heat capacity (or electronic entropy) are functions of temperature. However, magnetic heat capacity C_m (or magnetic entropy ΔS_m) is related to temperature T and external field B. The lattice contribution and electronic contribution are independent of the magnetic field, whereas the present work focuses on the thermodynamic properties of alloy carbides with external field to explain experimental phenomenon. The subsequent work is to study the effect of external field on magnetic-field-induced thermodynamic properties of alloy carbides.

4.5.1. Magnetic-Field-Induced Heat Capacity, Magnetic Entropy and Magnetic Enthalpy

Chuang et al. [37] have described the intrinsic magnetic heat capacity of pure iron over a wide temperature range, which coincided well with the experimental data. The expressions of C_m (Supplementary note 3) are now extended and the external magnetic field is considered in this work.

The C_m of carbides is displayed in Figure 6 with and without a magnetic field. Figure 6a,b show very promising results. Without an external field, the intrinsic magnetic heat capacity (dash lines) of η-Fe_2C and θ-Fe_3C agrees with the corresponding theoretical data [35]. Below T_c, the intrinsic magnetic heat capacity (dash lines) increases gradually. Near T_c, the intrinsic magnetic heat capacity reaches a maximum. Then, the intrinsic magnetic heat capacity decreases with increasing temperature and slowly approaches zero. The intrinsic and magnetic-field-induced magnetic heat capacity of η-Fe_2C, θ-Fe_3C, $Fe_{23}C_6$ and $Fe_{20}Cr_3C_6$ reaches a peak near T_c (B), due to the destruction of long-range order. It is noteworthy that the peaks of the magnetic-field-induced magnetic heat capacity (dotted and solid lines) shift to right with an external magnetic field. Below T_c, a magnetic field has little effect on C_m. In contrast to the intrinsic magnetic heat capacity (dash lines) in Figure 6, the magnetic-field-induced magnetic heat capacity will change significantly with the magnetic field over a wide range near T_c, relating to the stabilization of the magnetic field to ferromagnetic range (Section 4.4).

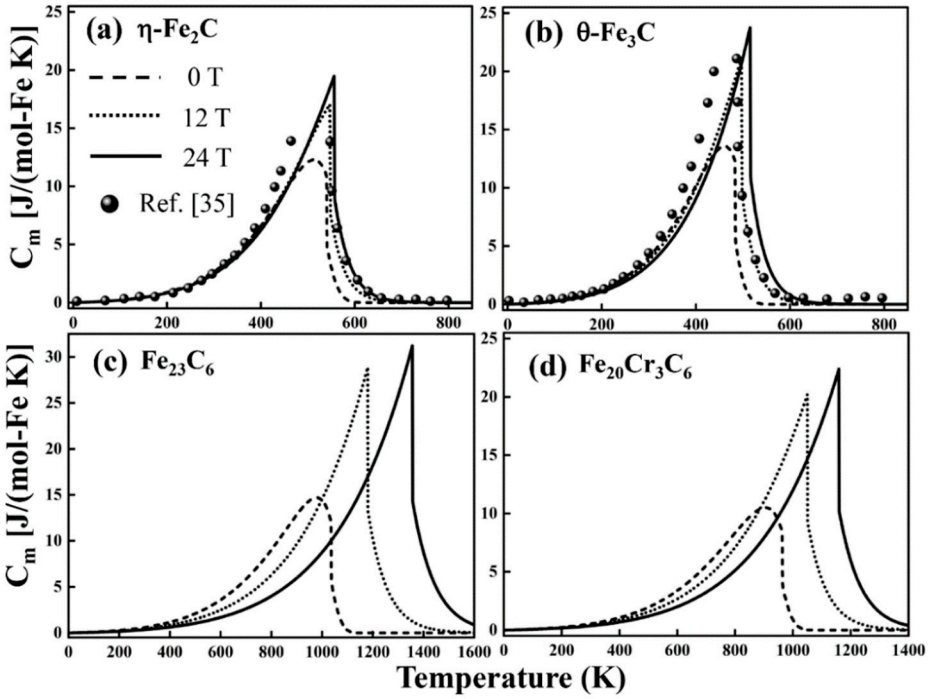

Figure 6. The magnetic-field-induced heat capacity of carbides with (dotted and solid lines) and without (dash lines) magnetic fields. (**a**) η-Fe_2C and reference data (ball symbols) [35], which were obtained in the absence of a magnetic field; (**b**) θ-Fe_3C and reference data (ball symbols) [35]; (**c**) $Fe_{23}C_6$; (**d**) $Fe_{20}Cr_3C_6$.

The magnetic entropy change $\Delta S_m(T, B)$ is presented in Figure 7. In the low temperature range, the magnetic field has little effect on the magnetic-field-induced magnetic entropy change $\Delta S_m(T, 12)$ and $\Delta S_m(T, 24)$ of η-Fe_2C and θ-Fe_3C (Figure 7a,b), whereas near T_c, there is a significant difference between the intrinsic and magnetic-field-induced magnetic entropy change of η-Fe_2C and θ-Fe_3C. For $Fe_{23}C_6$ and $Fe_{20}Cr_3C_6$ (Figure 7c,d), the curves are approximately coincident below 300 K. When the temperature is above 300 K, the magnetic-field-induced magnetic entropy change of $Fe_{23}C_6$ and $Fe_{20}Cr_3C_6$ are quite different from the intrinsic magnetic entropy change. Magnetic entropy is the degree of chaos caused by spin electrons. The peak value of $\Delta S_m(T, B)$ is associated with the ferromagnetic transition of carbides. At T_c, ferromagnet translates into a paramagnet, resulting in

a maximum $\Delta S_m(T,B)$. The maximum will increase with increasing magnetic field intensity. When the temperature is above T_c, the magnetic-field-induced magnetic entropy change is not zero due to the short-range order of the magnetic moment.

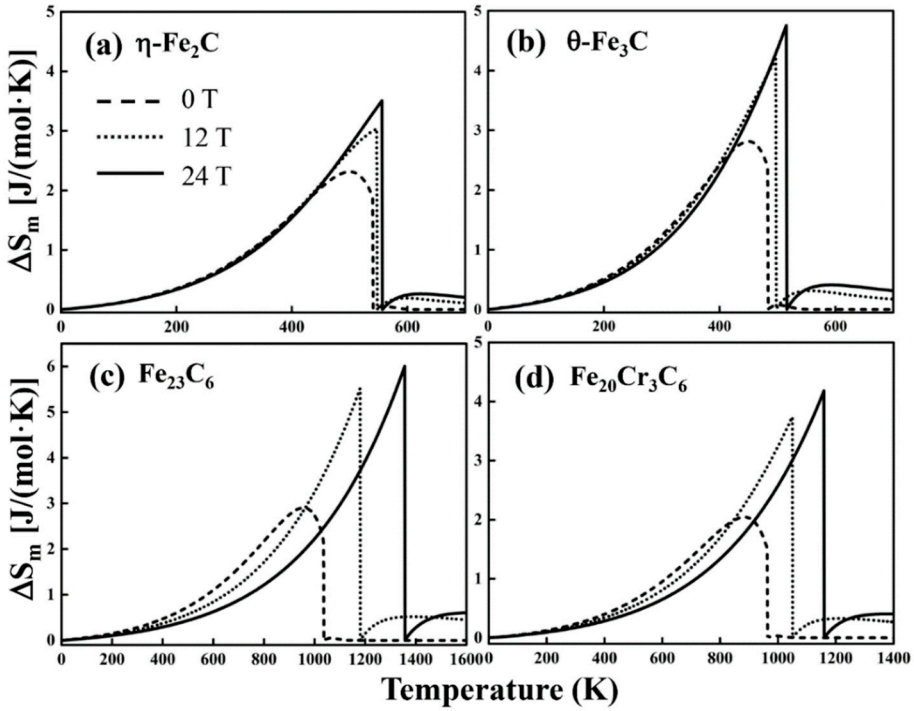

Figure 7. The magnetic-field-induced entropy changes of (**a**) η-Fe_2C, (**b**) θ-Fe_3C, (**c**) $Fe_{23}C_6$ and (**d**) $Fe_{20}Cr_3C_6$ with and without a magnetic field.

The magnetic enthalpy change $\Delta H_m(T,B)$ is shown in Figure 8. $\Delta H_m(T,B)$ increases when the temperature is lower than T_c. Near T_c, $\Delta H_m(T,B)$ exhibits the maximum magnetic enthalpy change. Then, $\Delta H_m(T,B)$ tends to stabilize with increasing temperature. Below T_c, the introduction of a magnetic field may not make a difference over a wide temperature range (approximately 0~500 K for η-Fe_2C, 0~450 K for θ-Fe_3C, and 0~400 K for both $Fe_{23}C_6$ and $Fe_{20}Cr_3C_6$). In other words, the magnetic-field-induced magnetic enthalpy change is mainly related to temperature in the low temperature range. Above T_c, the external field has a considerable effect on $\Delta H_m(T,B)$ because the magnetic field enhanced the coupling of the short-range magnetic moment. The magnetic-field-induced magnetic enthalpy changes of carbides increase as the magnetic field strength increases. This phenomenon suggests that magnetic-field-induced magnetism exerts an important influence on $\Delta H_m(T,B)$ when the temperature is above T_c. Essentially, the increase in the magnetic enthalpy change would increase the magnetic internal energy.

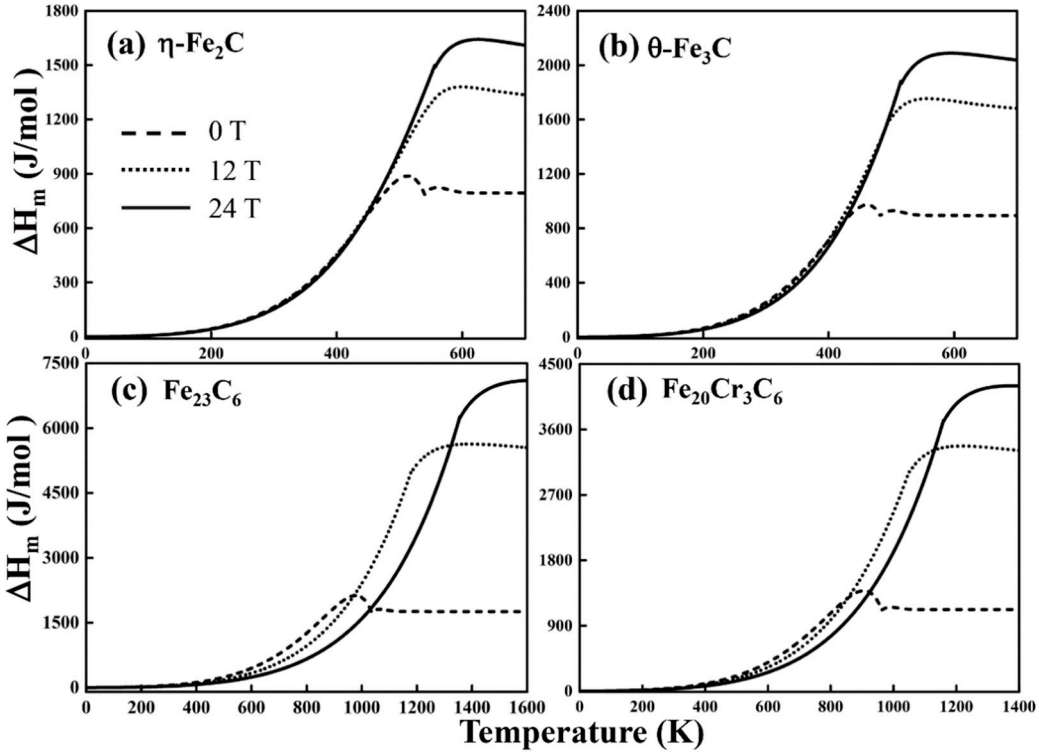

Figure 8. The magnetic-field-induced enthalpy changes of (**a**) η-Fe_2C, (**b**) θ-Fe_3C, (**c**) $Fe_{23}C_6$ and (**d**) $Fe_{20}Cr_3C_6$ with and without a magnetic field.

4.5.2. Gibbs Free Energy and Stability

In the traditional heat treatment process, it was found that carbides M_2C, M_3C, M_7C_3, $M_{23}C_6$ and M_6C are the common precipitate types in the 2.25Cr-Mo steel during tempering [38,39]. However, M_6C precipitates are rarely observed because they require a longer tempering time and at the expense of M_2C [38]. Experiments and theoretical demonstrations [16] showed that the precipitation order of carbides in the 2.25Cr-Mo steel is: $M_3C \rightarrow M_2C + M_3C \rightarrow M_7C_3 + M_2C + M_3C \rightarrow M_{23}C_6 + M_7C_3 + M_2C + M_3C$.

The stability of carbides under the magnetic field can be determined by magnetic Gibbs free energy (ΔG_m). ΔG_m was obtained by mathematical operations on magnetic entropy and magnetic enthalpy. Figure 9 shows the magnetic-field-induced magnetic free energy changes with a 12 T magnetic field. The negative value of ΔG_m (Figure 9) suggests that the three carbides are stable with the 12 T magnetic field. Under the experimental conditions, the magnetic-field-induced free energy change of $Fe_{20}Cr_3C_6$ is the lowest. ΔG_m of η-Fe_2C and θ-Fe_3C are zero near the experimental temperature because η-Fe_2C (T_c (0) = 540 K and T_c (12 T) = 547 K) and θ-Fe_3C (T_c (0) = 483 K and T_c (12 T) = 497 K) are already paramagnetic. The magnetic field has little effect on the magnetic-field-induced magnetic free energy of η-Fe_2C and θ-Fe_3C at the experimental temperature. ΔG_m of $Fe_{20}Cr_3C_6$ is approximately −58 J/mol under the experimental conditions, which agrees well with the obtained experiments.

In order to estimate the contribution of the magnetic field to the total free energy, the thermal free energy (($\Delta G\ (x, T)$ is also calculated. The thermal free energy is the function of the chemical composition x and temperature T. To explore the thermal contribution of the total free energy ($\Delta G_{\text{tot}}\ (x, T, B) = \Delta G\ (x, T) + \Delta G_m\ (T, B)$ the thermal energy is determined by MTDATA [40]. MTDATA can anticipate the equilibrium phases at different temperatures. The major controlling factor (R) [5,41] is introduced to evaluate the contribution of the magnetic field. R (%) is defined as the ratio of $\Delta G_m\ (T, B)$ to $\Delta G_{\text{tot}}\ (x, T, B)$, as shown in Equation (3).

$$\mathrm{R} = \left(\Delta G_m\ (T, B) / \Delta G_{\text{tot}}\ (x, T, B)\right) \times 100\% \quad (3)$$

As shown in Figure 10, R decreases as the temperature increases. Moreover, the R value of $Fe_{20}Cr_3C_6$ is the largest at the experimental temperature, which means that the magnetic contribution of $Fe_{20}Cr_3C_6$ is the most significant among η-Fe_2C, θ-Fe_3C and $Fe_{20}Cr_3C_6$. The calculating result indicated that the external-field-induced free energy will lower the total free energy of alloy carbides, thus changing the stability of carbides and altering the precipitation of carbides. The magnetic-field-induced free energy causes $M_{23}C_6$ ($Fe_{20}Cr_3C_6$) to precipitate in advance, which is consistent to the experiment result (as illustrated in Section 2).

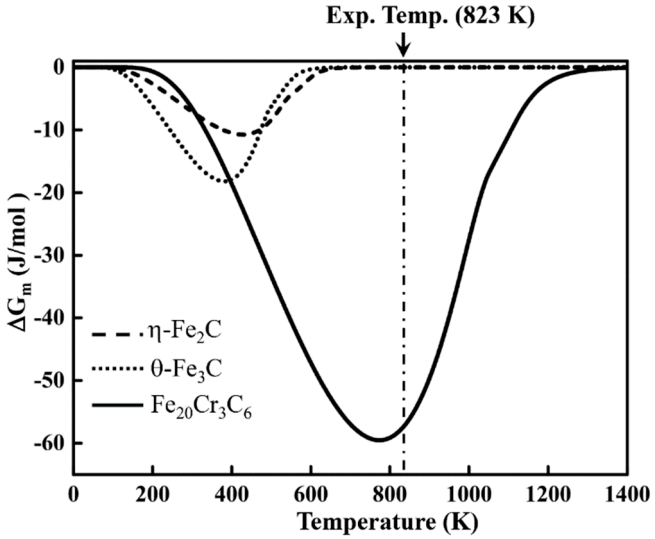

Figure 9. Magnetic-field-induced free energy change of η-Fe_2C, θ-Fe_3C and $Fe_{20}Cr_3C_6$ with a 12 T external field.

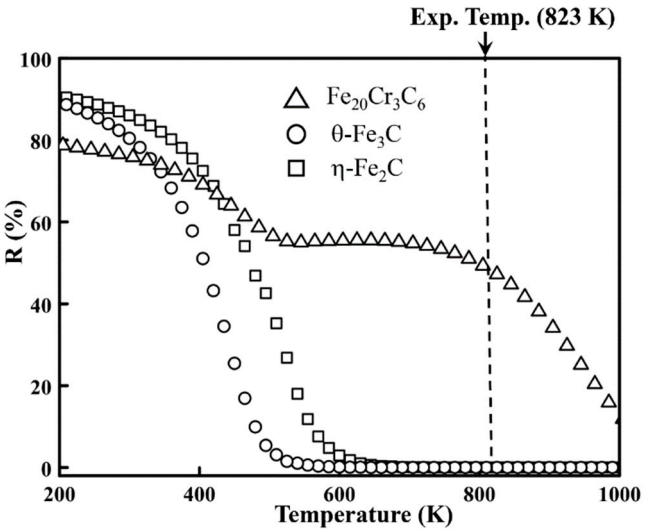

Figure 10. The major controlling factors of η-Fe_2C, Fe_3C and $Fe_{20}Cr_3C_6$ with the 12 T magnetic field.

5. Conclusions

The thermodynamic properties of carbides (η-Fe_2C, θ-Fe_3C, $Fe_{23}C_6$ and $Fe_{20}Cr_3C_6$) have been evaluated by a hybrid method combining the first-principles calculations, Weiss molecular field theory and thermal equilibrium software (MTDATA). The relationship between the magnetic moment and crystal structure was explored. Then, the Curie temperature and thermodynamic parameters were evaluated. The results provide an explanation of the experimental results that $M_{23}C_6$ precipitates in advance during medium-temperature tempering in the presence of an external field. The external field exerts a notable influence on carbide precipitation. The conclusions are as follows:

(1) $Fe_{23}C_6$ and $Fe_{20}Cr_3C_6$ have large magnetic moments, which are related to their NaCl-like structure. Antiparallel magnetic moments of Cr atoms weaken the total magnetic moment of $Fe_{20}Cr_3C_6$ by altering the exchange interaction.

(2) The Curie temperature change increases with the increasing magnetic field intensity. There are more Fe atoms in $Fe_{23}C_6$ and $Fe_{20}Cr_3C_6$, and the interaction is enhanced by the magnetic field, which obviously influences the Curie temperature.

(3) The magnetic heat capacity, magnetic entropy change and magnetic enthalpy change depend on the temperature and external field strength. Below the Curie temperature, the magnetic thermodynamic parameters rely more on the temperature than the magnetic field. Near or above the Curie temperature, the long-range order is destroyed, and the magnetic field increases the coupling of the short-range magnetic order, which increases the magnetic entropy change and magnetic enthalpy change significantly as the external field increases.

(4) The magnetic free energy of $Fe_{20}Cr_3C_6$ is the lowest among η-Fe_2C, θ-Fe_3C and $Fe_{20}Cr_3C_6$. The contribution of the 12 T magnetic field stabilizes $Fe_{20}Cr_3C_6$ by reducing the magnetic Gibbs free energy.

Supplementary Materials: The following are available online at http://www.mdpi.com/2075-4701/9/8/909/s1, Table S1: Parameters of C, Cr and Fe in the atomic scattering factor analytical formula.

Author Contributions: Conceptualization, T.H.; Formal analysis, Z.L., G.W. and H.L.; Funding acquisition, K.W.; Investigation, Z.L. and T.H.; Methodology, T.H. and K.W.; Project administration, K.W.; Resources, K.W.; Software, Z.L. and H.L.; Validation, T.H.; Visualization, Z.L. and G.W.; Writing—original draft, Z.L.; Writing—review and editing, T.H., K.W. and H.L.

Funding: This research was funded by the National Natural Science Foundation of China (Grant Nos. U1532268 and 11404249), State Key Laboratory of Refractories and Metallurgy (Grant No. 2018QN01), Hubei Province Key Laboratory of Systems Science in Metallurgical Process (Grant No. Z201701), State Scholarship Fund (Grant No. 201308420389), Wuhan Science and Technology Program (Grant No. 2019010701011382) and the 111 Project. The work was carried out at the National Supercomputer Centre in Tianjin, and the calculations were performed on TianHe–1 (A).

Conflicts of Interest: The authors declare no conflict of interest.

References

1. Zhang, Y.; Zhao, X.; Bozzolo, N.; He, C.; Zuo, L.; Esling, C. Low temperature tempering of a medium carbon steel in high magnetic field. *ISIJ Int.* **2005**, *45*, 913–917. [CrossRef]
2. Hou, T.P.; Li, Y.; Zhang, J.J.; Wu, K.M. Effect of magnetic field on the carbide precipitation during tempering of a molybdenum-containing steel. *J. Magn. Magn. Mater.* **2012**, *324*, 857–861. [CrossRef]
3. Zhou, Z.N.; Wu, K.M. Molybdenum carbide precipitation in an Fe-C-Mo alloy under a high magnetic field. *Scr. Mater.* **2009**, *61*, 670–673. [CrossRef]
4. Hou, T.P.; Wu, K.M. Alloy carbide precipitation in tempered 2.25 Cr-Mo steel under high magnetic field. *Acta Mater.* **2013**, *61*, 2016–2024. [CrossRef]
5. Hou, T.P.; Li, Y.; Wu, K.M.; Peet, M.J.; Hulme-Smith, C.N.; Guo, L. Magnetic-field-induced magnetism and thermal stability of carbides $Fe_{6-x}Mo_xC$ in molybdenum-containing steels. *Acta Mater.* **2016**, *102*, 24–31. [CrossRef]
6. Zhang, Y.; Gey, N.; He, C.; Zhao, X.; Zuo, L.; Esling, C. High temperature tempering behaviors in a structural steel under high magnetic field. *Acta Mater.* **2004**, *52*, 3467–3474. [CrossRef]
7. Xia, Z.X.; Zhang, C.; Lan, H.; Liu, Z.Q.; Yang, Z.G. Effect of magnetic field on interfacial energy and precipitation behavior of carbides in reduced activation steels. *Mater. Lett.* **2011**, *65*, 937–939. [CrossRef]
8. Hou, T.P.; Wu, K.M. The effect of high magnetic field on metal solute substitution in $M_{23}C_6$ alloy carbide. *Scr. Mater.* **2012**, *67*, 609–612. [CrossRef]
9. Hou, T.P.; Wu, K.M.; Liu, W.M.; Peet, M.J.; Hulme-Smith, C.N.; Guo, L.; Zhuang, L. Magnetism and high magnetic-field-induced stability of alloy carbides in Fe-based materials. *Sci. Rep.* **2018**, *8*, 3049. [CrossRef]
10. Talebi, S.H.; Jahazi, M.; Melkonyan, H. Retained austenite decomposition and carbide precipitation during isothermal tempering of a medium-carbon low-alloy bainitic steel. *Materials* **2018**, *11*, 1441. [CrossRef]

11. Pilling, J.; Ridley, N. Tempering of 2.25 pct Cr-1 pct Mo low carbon steels. *Metall. Trans. A* **1982**, *13*, 557–563. [CrossRef]
12. Fang, C.M.; Huis, M.A.V.; Sluiter, M.H.F. Formation, structure and magnetism of the γ-$(Fe,M)_{23}C_6$ (M = Cr, Ni) phases: A first-principles study. *Acta Mater.* **2016**, *103*, 273–279. [CrossRef]
13. Han, J.J.; Wang, C.P.; Liu, X.J.; Wang, Y.; Liu, Z.K. First-principles calculation of structural, mechanical, magnetic and thermodynamic properties for gamma-$M_{23}C_6$ (M = Fe, Cr) compounds. *J. Phys. Condens. Matter* **2012**, *24*, 505503. [CrossRef]
14. Fang, C.M.; Huis, M.A.V.; Sluiter, M.H.F.; Zandbergen, H.W. Stability, structure and electronic properties of γ-$Fe_{23}C_6$ from first-principles theory. *Acta Mater.* **2010**, *58*, 2968–2977. [CrossRef]
15. Yu, J. Carbide stability diagrams in 2.25Cr-1Mo steels. *Metall. Trans. A* **1989**, *20*, 1561–1564. [CrossRef]
16. Fujita, N.; Bhadeshia, H.K.D.H. Modelling simultaneous alloy carbide sequence in power plant steels. *ISIJ Int.* **2002**, *42*, 760–769. [CrossRef]
17. Westgren, A. Complex chromium and iron carbides. *Nature* **1933**, *132*, 480. [CrossRef]
18. Bowman, A.L.; Arnold, G.P.; Storms, E.K.; Nereson, N.G. The crystal structure of $Cr_{23}C_6$. *Acta Cryst.* **1972**, *28*, 3102–3103. [CrossRef]
19. Kohn, W.; Becke, A.D.; Parr, R.G. Density functional theory of electronic structure. *J. Phys. Chem.* **1996**, *100*, 12974–12980. [CrossRef]
20. Kresse, G.; Hafner, J. Ab initiomolecular dynamics for liquid metals. *Phys. Rev. B* **1993**, *47*, 558–561. [CrossRef]
21. Kresse, G.; Hafner, J. Ab initiomolecular-dynamics simulation of the liquid-metal-amorphous-semiconductor transition in germanium. *Phys. Rev. B* **1994**, *49*, 14251–14269. [CrossRef]
22. Kresse, G.; Furthmüller, J. Efficiency of ab-initio total energy calculations for metals and semiconductors using a plane-wave basis set. *Comput. Mater. Sci.* **1996**, *6*, 15–50. [CrossRef]
23. Amador, C.; Lambrecht, W.R.L.; Segall, B. Application of generalized gradient-corrected density functionals to iron. *Phys. Rev. B* **1992**, *46*, 1870–1873. [CrossRef]
24. Perdew, J.P.; Burke, K.; Ernzerhof, M. Generalized gradient approximation made simple. *Phys. Rev. Lett.* **1996**, *77*, 3865–3868. [CrossRef]
25. Monkhorst, H.J.; Pack, J.D. Special points for brillouin-zone integrations. *Phys. Rev. B* **1976**, *13*, 5188–5192. [CrossRef]
26. Souissi, M.; Sluiter, M.H.F.; Matsunaga, T.; Tabuchi, M.; Mills, M.J.; Sahara, R. Effect of mixed partial occupation of metal sites on the phase stability of gamma-$Cr_{23-x}Fe_xC_6$ (x = 0-3) carbides. *Sci. Rep.* **2018**, *8*, 7279. [CrossRef]
27. Lv, Z.Q.; Sun, S.H.; Jiang, P.; Wang, B.Z.; Fu, W.T. First-principles study on the structural stability, electronic and magnetic properties of Fe_2C. *Comput. Mater. Sci.* **2008**, *42*, 692–697. [CrossRef]
28. Faraoun, H.I.; Zhang, Y.D.; Esling, C.; Aourag, H. Crystalline, electronic, and magnetic structures of θ-Fe_3C, χ-Fe_5C_2, and η-Fe_2C from first principle calculation. *J. Appl. Phys.* **2006**, *99*, 093508. [CrossRef]
29. Medvedeva, N.I.; Aken, D.C.V.; Medvedeva, J.E. Stability of binary and ternary $M_{23}C_6$ carbides from first principles. *Comput. Mater. Sci.* **2015**, *96*, 159–164. [CrossRef]
30. Chong, X.; Jiang, Y.; Feng, J. Exploring the intrinsic ductile metastable Fe-C compounds: Complex chemical bonds, anisotropic elasticity and variable thermal expansion. *J. Alloys Compd.* **2018**, *745*, 196–211. [CrossRef]
31. Liu, Y.; Jiang, Y.; Xing, J.; Zhou, R.; Feng, J. Mechanical properties and electronic structures of $M_{23}C_6$ (M = Fe, Cr, Mn)-type multicomponent carbides. *J. Alloys Compd.* **2015**, *648*, 874–880. [CrossRef]
32. Weiss, P. L'hypothèse du champ moléculaire et la propriété ferromagnétique. *J. Phys. Théor. Appl.* **1907**, *6*, 661–690. [CrossRef]
33. Liu, X.J.; Fang, Y.M.; Wang, C.P.; Ma, Y.Q.; Peng, D.L. Effect of external magnetic field on thermodynamic properties and phase transitions in Fe-based alloys. *J. Alloys Compd.* **2008**, *459*, 169–173. [CrossRef]
34. Takahashi, C.; Ogura, M.; Akai, H. First-principles calculation of the curie temperature slater-pauling curve. *J. Phys. Condens. Matter* **2007**, *19*, 365233. [CrossRef]
35. Fang, C.M.; Sluiter, M.H.; Huis, M.A.V.; Ande, C.K.; Zandbergen, H.W. Origin of predominance of cementite among iron carbides in steel at elevated temperature. *Phys. Rev. Lett.* **2010**, *105*, 055503. [CrossRef]
36. Strässle, T.; Furrer, A.; Hossain, Z.; Geibel, C. Magnetic cooling by the application of external pressure in rare-earth compounds. *Phys. Rev. B* **2003**, *67*, 054407. [CrossRef]

37. Chung, Y.; Schmid, R.; Chang, Y.A. Magnetic contributions to the thermodynamic functions of pure Ni, Co, and Fe. *Metall. Trans. A* **1985**, *16*, 153–165. [CrossRef]
38. Thomson, R.C.; Bhadeshia, H.K.D.H. Changes in chemical composition of carbides in 2.25Cr-1Mo power plant steel part 1 bainitic microstructure. *Mater. Sci. Technol.* **1994**, *10*, 193–203. [CrossRef]
39. Tao, P.; Zhang, C.; Yang, Z.; Hiroyuki, T. Evolution and coarsening of carbides in 2. 25Cr-1Mo steel weld metal during high temperature tempering. *J. Iron Steel Res. Int.* **2010**, *17*, 74–78. [CrossRef]
40. Davies, R.H.; Dinsdale, A.T.; Gisby, J.A.; Robinson, J.; Martin, S.M. Mtdata-thermodynamic and phase equilibrium software from the national physical laboratory. *Calphad* **2002**, *26*, 229–271. [CrossRef]
41. Hou, T.P.; Peet, M.J.; Hulme-Smith, C.N.; Wu, K.M.; Li, Y.; Guo, L. The determining role of magnetic field in iron and alloy carbide precipitation behaviors under the external field. *Scr. Mater.* **2016**, *120*, 76–79. [CrossRef]

© 2019 by the authors. Licensee MDPI, Basel, Switzerland. This article is an open access article distributed under the terms and conditions of the Creative Commons Attribution (CC BY) license (http://creativecommons.org/licenses/by/4.0/).